Research article

Efficient photocatalytic bactericidal performance of green-synthesised TiO$_2$/reduced graphene oxide using banana peel extracts

Maisari Utami [a,*], Tong Woei Yenn [b], Mir Waqas Alam [c], Balasubramani Ravindran [d,e], Husniati [f], Indra Purnama [g,h], Salmahaminati [a], Habibi Hidayat [a], Faustine Naomi Dhetaya [a], Siva Nur Salsabilla [a]

[a] Department of Chemistry, Faculty of Mathematics and Natural Sciences, Universitas Islam Indonesia, Yogyakarta, 55584, Indonesia
[b] Institute of Medical Science Technology, Universiti Kuala Lumpur, Kajang, 43000, Malaysia
[c] Department of Physics, College of Science, King Faisal University, Al-Ahsa, 31982, Saudi Arabia
[d] Department of Medical Biotechnology and Integrative Physiology, Institute of Biotechnology, Saveetha School of Engineering, Saveetha Institute of Medical and Technical Sciences, Chennai, 602105, India
[e] Department of Environmental Energy and Engineering, Kyonggi University, Gyeonggi-Do, 16227, Republic of Korea
[f] Research Center for Pharmaceutical Ingredients and Traditional Medicine, Research Organization for Health, National Research and Innovation Agency (BRIN), South Tangerang, 15314, Indonesia
[g] Department of Agrotechnology, Faculty of Agriculture, Universitas Lancang Kuning, Pekanbaru, 28266, Indonesia
[h] Graduate School of Agricultural Sciences, Universitas Lancang Kuning, Pekanbaru, 28266, Indonesia

ARTICLE INFO

ABSTRACT

In this study, the fabrication of titanium dioxide/reduced graphene oxide (TiO$_2$/rGO) utilising banana peel extracts (*Musa paradisiaca* L.) as a reducing agent for the photoinactivation of *Escherichia coli* (*E. coli*) and *Staphylococcus aureus* (*S. aureus*) was explored. The GO synthesis was conducted using a modified Tour method, whereas the production of rGO involved banana peel extracts through a reflux method. The integration of TiO$_2$ into rGO was achieved via a hydrothermal process. The successful synthesis of TiO$_2$/rGO was verified through various analytical techniques, including X-ray diffraction (XRD), gas sorption analysis (GSA), Fourier-transform infrared (FT-IR) spectroscopy, ultraviolet–visible diffuse reflectance spectroscopy (UV–Vis DRS), scanning electron microscope-energy dispersive X-ray (SEM-EDX) and transmission electron microscopy (TEM) analyses. The results indicated that the hydrothermal-assisted green synthesis effectively produced TiO$_2$/rGO with a particle size of 60.5 nm. Compared with pure TiO$_2$, TiO$_2$/rGO demonstrated a reduced crystallite size (88.505 nm) and an enhanced surface area (22.664 m^2/g). Moreover, TiO$_2$/rGO featured a low direct bandgap energy (3.052 eV), leading to elevated electrical conductivity and superior photoconductivity. To evaluate the biological efficacy of TiO$_2$/rGO, photoinactivation experiments targeting *E. coli* and *S. aureus* were conducted using the disc method. Sunlight irradiation emerged as the most effective catalyst, achieving optimal inactivation results within 6 and 4 h.

1. Introduction

Bacterial water contamination by *E. coli* and *S. aureus* acts as a conduit for these bacteria to infect organisms. A method presently considered safe for degrading microorganisms involves photocatalysis, aided by reducing agents derived from biodegradable materials. This approach is deemed safer owing to its minimal generation of residual substances and its environmentally benign nature, employing substances that are non-harmful to the ecosystem [1].

Semiconductor titanium dioxide (TiO_2) is widely utilised in photocatalysis, favoured for its low toxicity, ready availability, cost-effectiveness, superior performance, high thermal stability and easy preparation [2]. Moreover, TiO_2 is recognised for its remarkable antibacterial properties [3]. Nevertheless, its application under natural sunlight is limited due to its considerable band gap—3.0 eV for the TiO_2 rutile phase and 3.2 eV for the TiO_2 anatase phase—restricting its activity primarily to the UV spectrum [4,5].

To augment the efficacy of TiO_2, various strategies involving metals, non-metals and carbon materials have been investigated. Among these, carbon allotropes have garnered substantial attention due to their exceptional electrical conductivity, extensive surface area, high thermal conductivity and remarkable mechanical strength. Incorporating carbon-based materials, particularly graphene, into TiO_2 modifications has resulted in composites exhibiting enhanced activity compared with pure TiO_2 [6,7]. This enhancement is attributed to the role of graphene as an electron acceptor, which helps mitigate electron-hole recombination during TiO_2 excitation, thereby improving performance of TiO_2 under visible light [8]. However, the hydrophobicity of graphene poses challenges in coupling metal oxides to its surface. A graphene derivative, reduced graphene oxide (rGO), retains similar characteristics to pure graphene but exhibits hydrophilicity, fewer oxygen groups and structural defects in its carbon framework [9]. Furthermore, rGO is known for its high antibacterial activity, which is ascribed to the generation of reactive oxygen species (ROS), such as hydroxyl radicals (OH•) and superoxide radicals ($\bullet O_2^-$), facilitating the degradation of organic pollutants and the inactivation of bacteria [10,11].

The synthesis of rGO involves a series of processes, including the oxidation of graphite, exfoliation and the subsequent reduction of graphene oxide. Akbar et al. emphasised that chemical reduction is recognised for its simplicity, cost-effectiveness and suitability for large-scale production [12]. Numerous reducing agents have been used for reducing GO, including hydrazine hydrate [13], $NaBH_4$ [14], $SOCl_2$ [15] and carbon monoxide [16]. Nevertheless, some of these chemicals are known for their toxicity and potential environmental hazards. Consequently, there is a pressing need to develop synthesis methods for rGO that are environmentally benign and utilise non-harmful materials.

Numerous studies have explored using eco-friendly reducing agents to convert GO to rGO, highlighting the shift towards environmentally sustainable methodologies. Yang et al. [17] utilised *Salvia spinosa*, a plant-based reducing agent, to examine its photothermal effects on pancreatic cancer cells. Bhattacharya et al. [18] employed aloe vera extract in the reduction process, aiming for dye removal applications. Mahjuddin and Ochiai [19] synthesised rGO using lemon juice as a reducing agent and applied it for the adsorption of methylene blue. Rani et al. [20] successfully produced green rGO nanosheets using lemon peel extracts (*Citrus limon*). Verastegui-Dominguez et al. [21] developed an environmentally friendly rGO using natural extracts from *Capsicum chinense* (Habanero) and *Larrea tridentata* (Gobernadora) for the degradation of methylene blue. Similarly, Buasuwan et al. [22] investigated the effectiveness of banana peel and juice extracts in reducing GO. Khojah et al. [23] explored the eco-friendly reduction of GO using mint extract, noting a more pronounced reduction effect than that achieved with *Tribulus terrestris* extract. Rai et al. [24] employed *Citrus maxima* (Pomelo) juice as a reducing agent for rGO synthesis, highlighting its potential use in supercapacitors. Finally, Mahmoud et al. [25] embarked on rGO synthesis using *Ziziphus spina-christi* extracts (Christ's thorn jujube) for catalysis, antimicrobial activity and antioxidant applications, demonstrating the versatility of plant-based reducing agents.

Bananas, tropical fruits with a substantial global production of approximately 48.9 MT [26], often lead to discarded peels post-consumption, representing an important source of unused waste. Banana peels are comprised 1.92%–3.25% pectin, a biocompatible and biodegradable heteropolysaccharide that serves as an effective reducing agent, facilitating oxidation-reduction reactions [27,28]. Phytochemical analyses, such as the one conducted by Velumani [29], reveal that banana peels (*Musa paradisiaca* L.*)* are rich in alkaloid and phenolic compounds, including tannins, saponins and flavonoids, endowing them with antioxidants and antibacterial properties. Buasuwan et al. [22] successfully harnessed a green reducing agent from banana peels and juice extract to reduce GO, efficiently eliminating oxygen-containing groups. Similarly, Olana et al. [30] synthesised a TiO_2/rGO nanocomposite utilising waste extracts from *Citrus sinensis* and *Musa acuminata* peels, demonstrating its effectiveness in the photocatalytic degradation of methylene blue.

In this study, GO was synthesised through a modified Tour method employing $KMnO_4$ with a mixture of H_2SO4 and H_3PO_4. This method offers an environmental advantage as it avoids the emission of toxic gases. The rGO was produced using a green reducing agent selected for its effective reduction of GO. Employing banana peel extracts as reducing agents to produce rGO epitomises an innovative approach to waste utilisation. This method presents a practical, cost-effective, non-toxic, biocompatible and environmentally benign pathway, leveraging the abundant availability of banana peels. To the best of our knowledge, research specifically dedicated to the synthesis of TiO_2/rGO nanocomposites using banana peel extracts as a reducing agent for the photoinactivation of *E. coli* and *S. aureus* remains unexplored. In this research endeavour, our study focuses on the potential activity of the TiO_2/rGO nanocomposite in effectively deactivating bacteria. This process harnesses sunlight energy for photocatalysis, offering a promising avenue for sustainable and efficient bacterial inactivation.

2. Materials and methods

2.1. Materials

Graphite powder, banana peel extracts, sulfuric acid 95% (H_2SO_4, Merck), potassium permanganate 99% ($KMnO_4$, Merck), hydrogen peroxide 30% (H_2O_2, Merck), hydrochloric acid 37% (HCl, Merck) and ethanol 99% (C_2H_5OH, Merck) were employed in this study. *E. coli* and *S. aureus* were employed with nutrient agar (NA), nutrient broth (NB) and Mueller Hinton broth (MHB), which were used for the biological investigations.

2.2. Material synthesis

2.2.1. Banana peel extraction

Here, 20 g of Kepok banana peels was mixed with 100 mL of distilled water and heated to 95 °C for 2 h. Next, the mixture was filtered using Whatman filter paper, and the resulting filtrate was collected in a glass bottle. Subsequently, the extract was stored in a refrigerator overnight [31].

2.2.2. Synthesis of GO

A 0.5 g of graphite was oxidised with 90 mL of H_2SO_4 and 10 mL of H_3PO_4. After adding 4.5 g of $KMnO_4$, the mixture was stirred for 8 h at 50 °C. Post-stirring, the mixture was allowed to settle and cool to room temperature. Subsequently, 250 mL of distilled water and 10 mL of 30% H_2O_2 were incrementally added to the mixture. The resultant solution was then filtered, and the collected precipitate was thoroughly washed with 100 mL of 5% HCl. This step was succeeded by another washing with 100 mL of deionised water. The mixture was then stirred at 60 °C for an additional 8 h. The end product, a paste of GO, was subsequently dried in an oven at 60 °C for 2 h, yielding GO powder [32].

2.2.3. Synthesis of rGO

The synthesis of rGO began with the dispersion of 0.1 g of GO in 30 mL of distilled water. This mixture was subjected to sonication for 30 min. Subsequently, 2 mL of banana peel extract was added to the mixture, then placed under reflux at a temperature of 95 °C for 5 h. Post-reflux, the solution was filtered to obtain a precipitate. This precipitate was thoroughly washed with 100 mL of deionised water to remove residual impurities. Finally, the washed precipitate was dried in an oven at 60 °C for 6 h, forming the rGO powder [33].

2.2.4. Synthesis of TiO$_2$/rGO

The TiO$_2$/rGO composite was synthesised utilising the hydrothermal method. Initially, 0.04 g of rGO was dissolved in a solvent mixture consisting of 80 mL of distilled water and 40 mL of ethanol. This mixture was then sonicated for 30 min. Next, 0.4 g of TiO$_2$ was added to the solution, followed by continuous stirring for 2 h to achieve a homogenous mixture. This mixture was subsequently transferred into an autoclave and subjected to a hydrothermal reaction by placing it in an oven maintained at 120 °C for 3 h. Next, the mixture was further stirred for an additional 2 h under UV and then filtered to collect the precipitate, which was thoroughly washed with distilled water. Finally, the washed precipitate was dried in an oven at 70 °C for 12 h, forming the TiO$_2$/rGO composite powder [34].

2.3. Study of photocatalytic activity

The efficacy of the photoinactivation test on bacteria was assessed using the disc diffusion method. Optimal concentrations of the TiO$_2$/rGO composite were determined by experimenting with different ratios of TiO$_2$/rGO to the medium, specifically NB. The concentration ratio used for *E. coli* bacteria was 1:1, converting the materials from a powder form to a solution form. For *S. aureus* bacteria, a concentration ratio of 1:9 was utilised. The effectiveness of photocatalysis was evaluated under three different types of light: UV light, sunlight and in the absence of irradiation, each at three different concentrations. After identifying the optimal type of light and concentration, the exposure times of 2 h, 4 h and 6 h were tested. The results obtained are the formation of clear zones on the media consisting of NA and MHB.

3. Results and discussion

3.1. Material characterisation

3.1.1. X-ray diffraction (XRD) characterisation

Diffractogram analysis was performed utilising a Bruker D2 Phaser (Germany) within a diffraction angle range of $2\theta = 2°–80°$ to generate distinctive peaks characteristic of each material. For the determination of crystal size, the Debye-Scherrer equation was employed, expressed as:

$$D = \frac{K\,\lambda}{\beta \cos\theta}$$

where D is the crystal size expressed in nanometers (nm), K is the crystal from factor constant (generally a value of 0.94 is used), λ is the wavelength of the X-ray radiation source (1.54056 Å), β states the value of full width at half maximum (FWHM) (rad) and θ as the diffraction angle (degree). The Debye-Scherrer equation elucidates that the calculated crystal size is inversely proportional to the FWHM value. Furthermore, the intensity of each crystal field substantially impacts the FWHM value, with a high intensity correlating to a reduced FWHM value. By incorporating the values of wavelength, intensity, 2θ and FWHM, derived from X-ray diffraction (XRD) test results, the Debye-Scherrer equation can be modified to facilitate the computation of crystal size [35].

The diffractogram peaks of the materials are depicted in Fig. 1. Both GO and rGO exhibit a low-intensity peak at 2θ = 10.03° (111), corresponding to a layer spacing of 0.879 nm. For GO, a broader peak is observed at 2θ = 42.53° (622), indicating a layer spacing of 0.2121 nm, while for rGO, a broadened peak appears at 2θ = 10.768° (111) with a layer spacing of 0.2104 nm, as denoted by JCPDS No. 01-082-2261. Turbostratic carbon, a unique class of carbon, exhibits structural ordering intermediate between amorphous carbon and crystalline graphite phases. This intermediate phase contributes to the indeterminate phase of GO, manifesting as a broadened band at the weak peak of 42.53° (622), as indicated by JCPDS No. 01-082-2261. Furthermore, the transformation from GO to rGO is temperature-dependent, broadening these bands [36]. The rGO peak is broader than that of GO, which retains sharper peaks. This broadening in rGO is attributed to the sonication process during the rGO formation, wherein GO undergoes exfoliation to yield rGO. The reduction in layer spacing from 0.879 nm to 0.2104 nm confirms the successful reduction of oxygen-containing groups and the synthesis of rGO.

TiO$_2$ and TiO$_2$/rGO exhibit distinct and pronounced diffractogram peaks. In TiO$_2$, the most substantial intensity is observed at 2θ = 27.481° (110), corresponding to an interlayer spacing of 0.3243 nm. Similarly, the peak with the highest intensity for TiO$_2$/rGO is noted at 2θ = 27.469° (110), reflecting an interlayer spacing of 0.3244 nm. The TiO$_2$ and TiO$_2$/rGO peaks show remarkable similarity, with only minor shifts. This resemblance is predominantly due to the substantial presence of TiO$_2$ within the TiO$_2$/rGO nanocomposite, sustaining a ratio of 1:10 (TiO$_2$:TiO$_2$/rGO). Analysing the diffractogram peaks, it is evident that GO and rGO present an amorphous phase, whereas TiO$_2$ and TiO$_2$/rGO are in a crystalline phase. The TiO$_2$/rGO nanocomposite's successful synthesis is evidenced using TiO$_2$ in the rutile phase, as confirmed by JCPDS No. 00-021-1276.

The Debye-Scherrer equation was applied for material crystal size determination with the mean crystal sizes for each sample are listed in Table 1. The average crystal size for GO is determined to be 7.983 nm, whereas for rGO, it is 5.707 nm. These results indicate that the crystal size of rGO is smaller than that of GO, attributed to the sonication process employed in synthesising rGO, where intensive ultrasonic activity contributes to particle size reduction. In the case of TiO$_2$, the average crystal size is measured at 83.375 nm. Conversely, the average crystal size for the TiO$_2$/rGO composite is slightly larger, at 88.505 nm. Typically, TiO$_2$ exhibits a smaller crystal size compared with the TiO$_2$/rGO composite. This disparity is primarily due to the synthesis process of TiO$_2$/rGO, wherein the combination of TiO$_2$ and rGO inhibits crystal growth.

3.1.2. Gas sorption analysis (GSA) characterisation

The surface area of materials was evaluated at 77 K through N$_2$ adsorption/desorption measurements using a Quantachrome Novatouch LX-4 (Austria). Fig. 2 illustrates the pore structure of the material, classified as type IV pores (mesopores) according to the IUPAC classification, evidenced by the hysteresis loops at high partial pressures and a pore size distribution ranging from 2 to 50 nm [37,38]. Based on the Barret-Joyner-Halenda method, the calculations revealed that the maximum pore size is predominantly at a radius of 2 nm, aligning with the observed pore size range of 2–50 nm. The surface area of the material was determined using the Brunauer-Emmett-Teller method, revealing a surface area of 39.735 m^2/g for GO and 47.354 m^2/g for rGO, as detailed in Table 2. The data indicate that the surface area of rGO is larger than that of GO, attributed to the reduction process involved in rGO synthesis, which enhances the material's surface area.
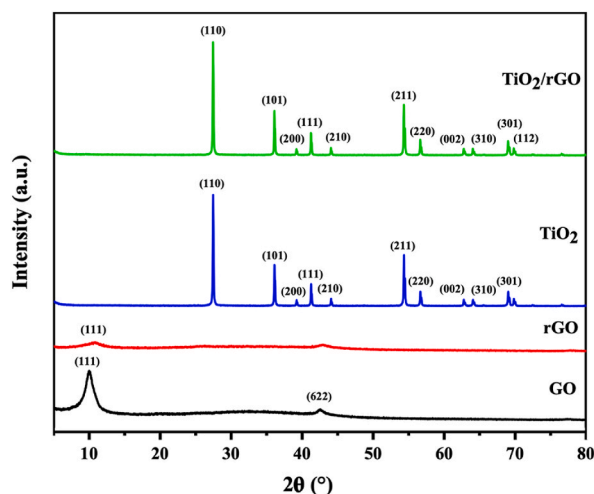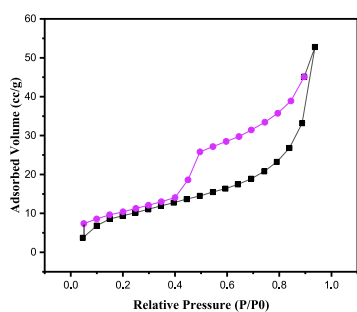

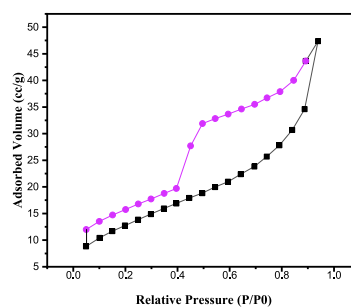**Fig. 1.** XRD patterns of materials.

Table 1
The average crystal size of materials.

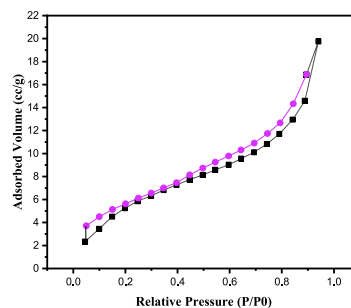| Sample	Layer spacing (nm)	D (nm)	Average D (nm)
GO	0.8794	6.822	7.983
	0.2121	9.144	
rGO	0.2104	5.707	5.707
TiO_2	0.3243	64.952	83.375
	0.2484	54.556	
	0.2185	6.012	
	0.1687	116.476	
	0.1624	109.314	
	0.1360	86.939	
TiO_2/rGO	0.3244	64.952	88.505
	0.2485	56.655	
	0.2186	69.074	
	0.1687	109.286	
	0.1683	116.478	
	0.1624	113.518	
	0.1360	89.573	
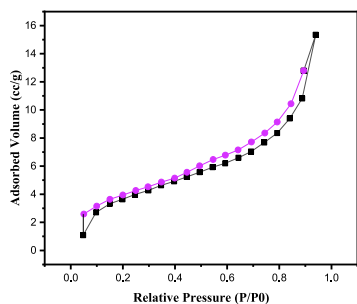
Fig. 2. Isotherm curve (a) GO, (b) rGO, (c) TiO_2 and (d) TiO_2/rGO.

Table 2
Textural properties of the materials.

Material	Surface area (m^2/g)	Total pore volume (cc/g)	Average pore size (nm)
GO	39.735	0.082	4.117
rGO	47.354	0.073	3.102
TiO_2	14.167	0.024	3.360
TiO_2/rGO	22.664	0.031	2.703

Youn et al. [39] investigated the oxidation state of GO in relation to the surface area of rGO sheets. The study revealed that GO had a higher oxidation state, indicating a substantial concentration of oxygen functional groups intercalated between the graphene layers. This condition facilitated the formation of rGO with an increased specific surface area. The expanded surface area of rGO emphasised the improved electrical conductivity, a consequence of the reduction process employing banana peel extracts. This enhanced electrical conductivity facilitates efficient electron transport during the photocatalytic process [40].

The surface area of TiO_2 is measured at 14.167 m^2/g, whereas that of TiO_2/rGO is determined to be 22.664 m^2/g. These results suggest that integrating rGO into TiO_2 impedes its agglomeration, thereby bestowing the TiO_2/rGO composite with a considerably larger surface area than TiO_2 [41]. The embedding of TiO_2 onto rGO is deemed a successful strategy, as it yields a more efficient photocatalytic material, largely attributed to the increased surface area facilitated by the rGO incorporation.

3.1.3. Fourier-transform infrared (FT-IR) characterisation

Functional groups in GO, rGO, TiO_2 and TiO_2/rGO materials were characterised through FT-IR analysis using UATR Spectrum Two PerkinElmer (United States). The FT-IR spectra were produced by associating wave numbers with transmittance values. Fig. 3 depicts the FT-IR spectrum for each material, highlighting the specific wave numbers corresponding to various functional groups. Table 3 details the functional groups discerned based on their respective wave numbers. The analysis of functional groups within GO materials reveals the presence of oxygen-containing functional groups. Notably, a peak at 586.97 cm^{-1} corresponds to the bending vibration of C–O–C, representing the epoxy group. Furthermore, a peak at 1224.23 cm^{-1} is attributed to the bending vibration of the C–OH hydroxyl group [42].

The peak at 1627.08 cm^{-1} signifies the stretching vibration of the sp^2 plane within the C–C bond. The peak at 3413.42 cm^{-1} is associated with the absorption of O–H groups, indicating the presence of a vibration band related to oxygen-binding functional groups, which suggests the oxidation of graphite [43]. For the rGO material, the peak at 1073.51 cm^{-1} denotes a stretching vibration of C–O bonds [44]. In addition, the peak at 1588.20 cm^{-1} corresponds to the absorption of C=C, and the peak at 1623.59 cm^{-1} indicates C–C absorption. Moreover, the peak at 1732.43 cm^{-1} is characteristic of the stretching vibration of C=O in carbonyl/carboxyl functionalities, and the peak at 3391.87 cm^{-1} is associated with the stretching vibration of O–H bonds present in water [45].

Analysis of functional groups within GO and rGO materials highlighted a more pronounced binding of carbon groups in rGO, attributable to reducing agents during rGO synthesis, which considerably contribute to carbon content. In rGO, alkene functional groups exhibited slight shifts, partly due to the inherent reduction process in rGO synthesis. The hydrophilic nature of rGO is elucidated by the prevalence of polar groups, predominantly hydroxyl functional groups, on the rGO surface. The diminished absorption intensity in rGO spectra reflects the successful removal of oxygen-containing functional groups, confirming the effective reduction of GO [46]. Furthermore, this reduction process not only augments electrical conductivity but also enhances material orientation by rectifying defects [40]. The TiO_2 spectrum demonstrates a distinctive absorption peak at 648.96 cm^{-1}, indicative of the characteristic vibrations of Ti–O–Ti bonds. In the TiO_2/rGO composite, an absorption shift is observed due to the formation of Ti–O–C bonds, causing the TiO_2 absorbance edge to migrate towards higher wavelength regions [47]. This notable shift in absorption indicates the predominance of successful bond formation, leading to a decrease in the absorption intensity of Ti–O–Ti bonds.

3.1.4. UV–Vis diffuse reflectance spectroscopy (DRS) characterisation

The determination of the band gap energy for both TiO_2 and TiO_2/rGO was conducted by analysing the UV–Vis DRS data from the Shimadzu UV-2401 PC (Japan). As illustrated in Fig. 4, the band gap energy of TiO_2/rGO, at 3.15 eV, is marginally narrower than that of TiO_2, which is 3.052 eV. This reduction is attributed to the integration of rGO within the energy gap of TiO_2, resulting in a redshift of the absorption edge from TiO_2 to TiO_2/rGO [48]. This observation aligns with the findings of Yu and Tang [49], who reported that incorporating rGO into TiO_2 leads to a decrease in the bandgap value, measuring 3.14 eV for TiO_2 and 3.07 eV for TiO_2-rGO. A
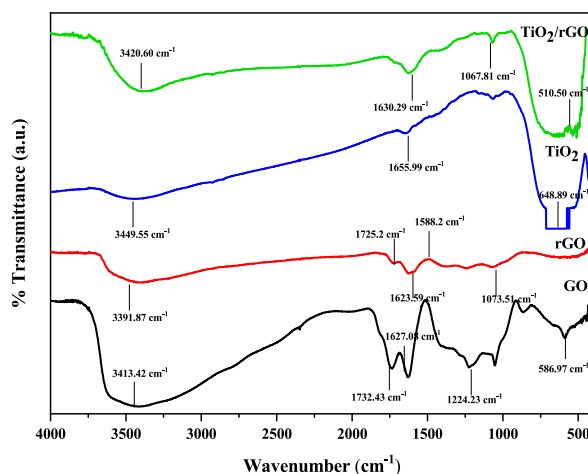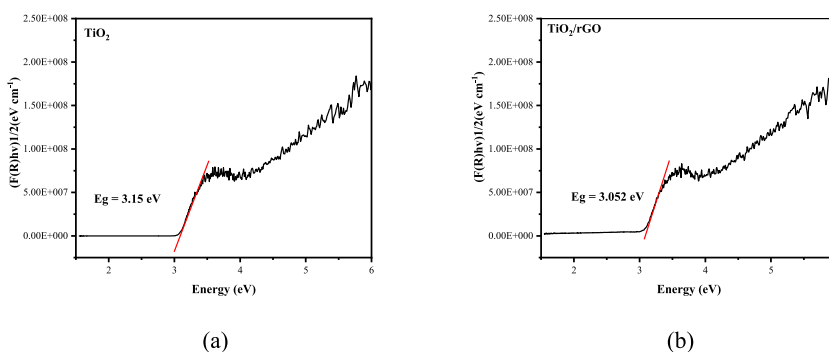

Fig. 3. FT-IR spectra of the materials.

Table 3
Functional groups of materials.

Sample	Wavenumbers (cm^{-1})	Functional groups
GO	3413.42	O–H
	1732.43	C=O
	1627.08	C–C
	1224.23	C–OH
	586.97	C–O–C
rGO	3391.87	O–H
	1725.20	C=O
	1623.59	C–C
	1588.20	C=C
	1073.51	C–O
TiO$_2$	3449.55	O–H
	1650.99	Ti–OH
	648.96	Ti–O–Ti
TiO$_2$/rGO	3420.60	O–H
	1630.29	C–C
	1067.81	C–O
	510.50	Ti–O–C

Fig. 4. Band gap energies of (a) TiO$_2$ and (b) TiO$_2$/rGO.

narrower band gap promotes electron transition from the valence band (lower energy level) to the conduction band (higher energy level), effectively minimising electron-hole recombination [50].

The intersection points on the graph depicting the relationship between $(\alpha h v)^2$ and photon energy (eV) serves as a determinant for the band gap value. This value correlates with absorption regions at different wavelengths. The band gap energy of TiO$_2$ is 3.15 eV, corresponding to a wavelength of 394 nm. Conversely, the TiO$_2$/rGO composite exhibits a marginally lower band gap energy of 3.052 eV, equivalent to a wavelength of 408 nm. Notably, TiO$_2$ demonstrates pronounced absorption within the ultraviolet spectrum (200–400 nm). Liu reported that the modification of rGO induces a broadening of light absorption, effectively shifting the absorption spectrum of TiO$_2$ towards the visible region (400–800 nm) [47]. These findings underscore that the modification of TiO$_2$ was successfully executed, substantially enhancing the capacity of TiO$_2$/rGO to absorb visible light efficiently compared to pristine TiO$_2$.

3.1.5. Scanning electron microscopy-energy dispersive X-ray (SEM-EDX) characterisation

The SEM analysis elucidates the surface characteristics of GO, rGO, TiO$_2$ and TiO$_2$/rGO materials, while the EDX analysis sheds light on the elemental composition of each material, utilising the JEOL JSM-6510LA (Japan). Fig. 5 depicts the morphology of each material at a magnification of 10,000x, showcasing distinctive features. The rGO exhibits a refined texture, resembling thinly coated flakes and appearing more diminutive relative to the GO material, which is characterised by its rough and bulky sheets [51,52]. The relatively coarse texture of the GO layer, as compared with rGO, originates from the presence of functional groups containing oxygen atoms, leading to surface distortions [53]. This observation underscores the successful synthesis of rGO, marked by a finer material layer.

The integration of the carboxyl functional group (–COOH), originating from pectin compounds in banana peel extracts, contributes to the successful synthesis of rGO by substituting the oxygen-containing groups with carbon. Morphologically, a marked distinction is evident between TiO$_2$ and TiO$_2$/rGO materials, as characterised by the appearance of distinct white lumps. For TiO$_2$, the surface presents an evenly distributed white layer. In contrast, the TiO$_2$/rGO exhibits a smoother texture, with the white lumps appearing agglomerated.

The elemental composition of each material was determined through EDX analysis, the results of which are detailed in Table 4. Specifically, for the GO material, the composition was found to consist solely of carbon and oxygen, without the presence of any other elements. This absence of extraneous elements indicates the high purity of the synthesised GO [54]. The carbon component in GO and
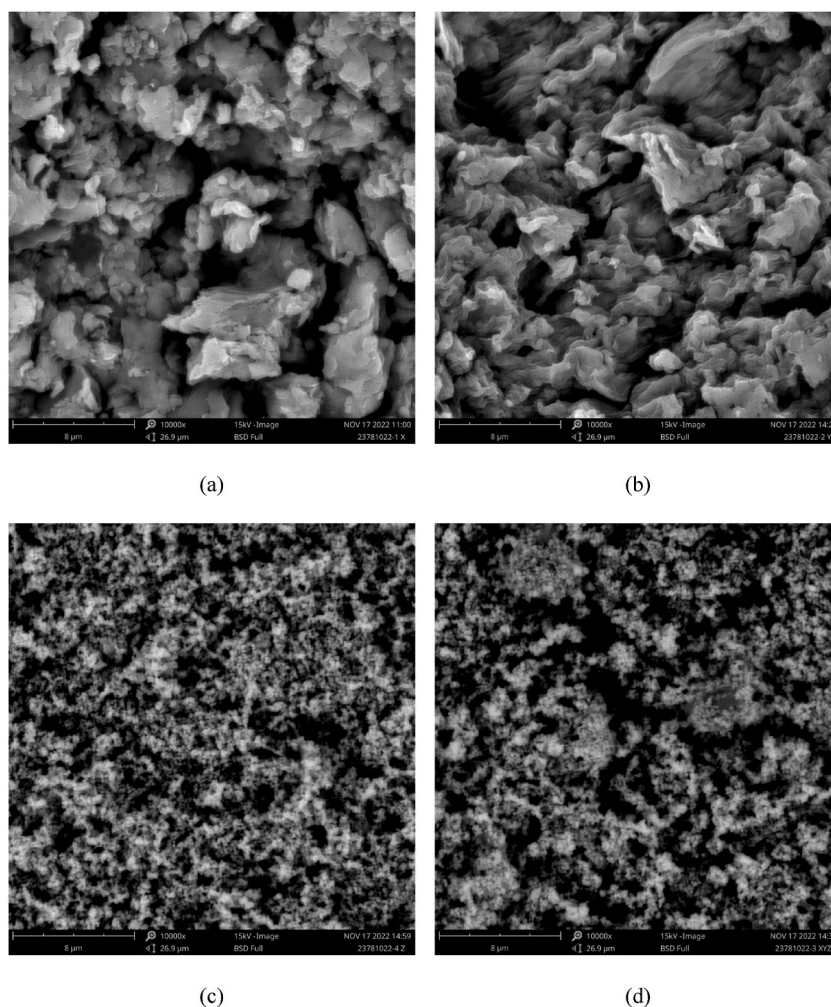
(a)   (b)

(c)   (d)

Fig. 5. Surface morphologies of (a) GO, (b) rGO, (c) TiO_2 and (d) TiO_2/rGO.

Table 4
Constituent elements present in materials.

Sample	Mass percentage (%)				
	C	O	Ti	K	Al
GO	70.08	29.92	–	–	–
rGO	75.2	24.48	–	0.32	–
TiO_2	6.26	71.1	20.69	–	1.36
TiO_2/rGO	21.01	59.61	18.07	–	1.31

rGO primarily originates from the graphite material used as the precursor in the synthesis of GO. However, the oxygen component is introduced during the oxidation process. Although both GO and rGO materials predominantly consist of carbon, the carbon content in rGO is higher than in GO. This increase is attributed to the reduction process of rGO synthesis, which effectively reduces the oxygen-containing groups. Moreover, introducing pectin as a reducing agent in the synthesis process contributes additional carbon to the rGO structure, effectively replacing some oxygen bonds with carbon.

In the rGO material, the presence of potassium is attributed to the banana peel extracts used as a reducing agent for graphene oxide [55]. For TiO_2, oxygen is the predominant element, followed by titanium and carbon. In contrast, the TiO_2/rGO composite primarily consists of oxygen, carbon and titanium [56]. The carbon content originates from the rGO sheet, whereas the titanium component is derived from the TiO_2 crystal. Oxygen is contributed by both the TiO_2 crystal and a small quantity of oxygen-containing groups on the rGO sheet [57]. A trace amount of aluminium is identified in both TiO_2/rGO and TiO_2, presumably stemming from the commercially sourced TiO_2. Although the purity of TiO_2 may not be fully guaranteed, the minor presence of aluminium does not impede the efficacy

of TiO$_2$ in the photocatalytic process. These observations confirm the successful integration of TiO$_2$ onto the rGO surface, evidenced by a reduction in the oxygen content coupled with an elevation in the carbon content in the TiO$_2$/rGO composite.

3.1.6. Transmission electron microscopy (TEM) characterisation

The TEM examination using JEOL JEM-1400 (Japan) yielded detailed insights into the particle morphology of GO, rGO, TiO$_2$ and TiO$_2$/rGO, as depicted in Fig. 6. The morphological features observed via TEM exhibit enhanced clarity and contrast than the surface morphology outcomes derived from SEM analysis. As presented in Fig. 6, both GO and rGO materials display a crumpled and layered morphology characterised by wavy sheets interconnected to form a network, primarily due to the substantial π-π interactions among the surfaces of the graphene layers [35]. Notably, the rGO material exhibits a more pronounced wrinkled texture and a thinner structure, which can be attributed to the removal of oxygen-containing groups [58]. The darker areas within the rGO morphology indicate an increased layer density, a feature attributed to the strong van der Waals forces interlinking each layer [36]. In contrast, the TiO$_2$ particles exhibit an irregular spherical morphology, characterised by pronounced agglomerations. Within the TiO$_2$/rGO composite, the TiO$_2$ clusters appear to be uniformly distributed and deposited on the delicate sheets of the rGO surface [59,60].

The TEM analysis underscored the heterogeneity in particle sizes across each material, as depicted in Fig. 7, discernible from the resultant non-uniform morphology. The mean particle size was determined to be 202.5 nm for TiO$_2$ and 60.5 nm for TiO$_2$/rGO. The predominance of TiO$_2$, in terms of particle size and mass percentage relative to rGO, engenders a propensity towards particle agglomeration. The synthesis outcome of the TiO$_2$/rGO composite indicates that the material qualifies as nanoparticles.

3.2. Photocatalytic activity

The photoinactivation process targeting *E. coli* was performed at a concentration ratio of 1:1, while the process targeting *S. aureus* was conducted at a concentration ratio of 1:9. In treatments devoid of radiation, relying solely on TiO$_2$/rGO material, it was observed that *E. coli* did not exhibit clear zone formation on the test plate. However, a clear zone measuring 5 mm was evident on the test plate for *S. aureus*, categorising it within a weak inhibition zone. This indicates that in the absence of energy from sunlight, TiO$_2$/rGO material is insufficiently effective against *E. coli* and *S. aureus*. Clear zones did not form around the discs in the unirradiated samples; however, the material's potential as a degrading agent was evident. This potential was indicated by the variation in colour and turbidity between the media surrounding the material and the media agent. This is attributed to the nature of TiO$_2$/rGO as a photocatalyst, which requires light to optimise its activity.

Notably, in Fig. 8, each different irradiation time interval is marked by a distinct clear zone. Specifically, irradiation for 2, 4 and 6 h resulted in clear zones with diameters of 22, 28 and 35 mm, respectively. The correlation between extended irradiation time and the enhanced elimination of *E. coli* bacteria is apparent. The increasing width of the clear zone indicates that 6 h of sunlight exposure is
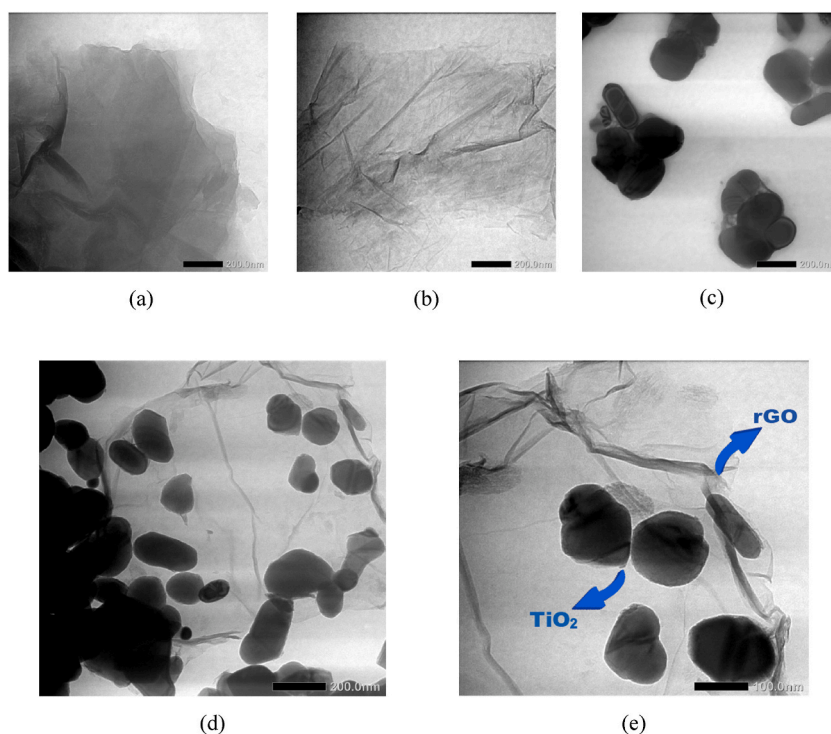

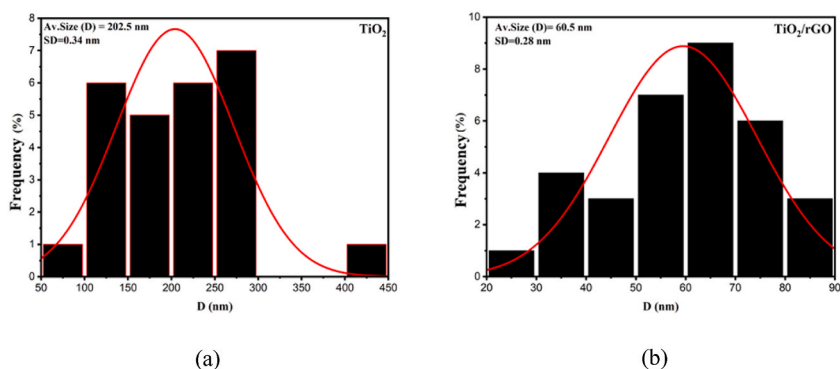Fig. 6. Internal morphologies of (a) GO, (b) rGO, (c) TiO$_2$, (d) TiO$_2$/rGO and (e) TiO$_2$/rGO with larger magnification.

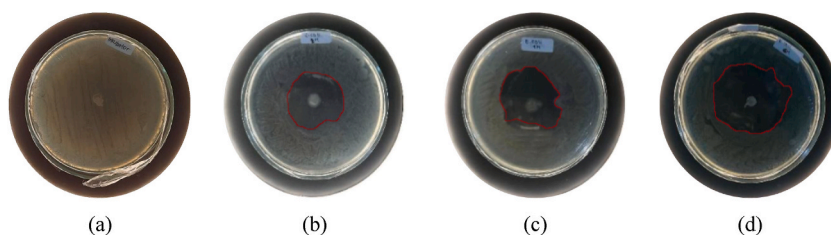**Fig. 7.** Histogram results of (a) TiO$_2$ and (b) TiO$_2$/rGO.

Fig. 8. Photocatalytic antibacterial process targeting *E. coli* (a) without irradiation and with varying durations of sunlight irradiation: (b) 2 h, (c) 4 h and (d) 6 h.

highly effective in degrading *E. coli*. This heightened efficacy over 6 h can be attributed to the prolonged interaction with *E. coli* bacteria, which are typically anaerobic and responsive to factors such as ambient air and adequate sunlight exposure. As a result, the bacterial plasma membrane becomes increasingly susceptible to damage, leading to the disruption of the DNA in *E. coli* cells.

Variations in irradiation time produce clear zones on *S. aureus* bacteria, as depicted in Fig. 9. After 2 h, 4 h and 6 h of irradiation, distinct clear zones measuring 20, 22 and 5 mm in diameter, respectively, are observed. *S. aureus* bacteria exhibit a rapid tendency to develop resistance against multiple antimicrobial agents. The most effective timeframe for inactivation is within 4 h, which is attributable to its gram-positive characteristics. These attributes encompass a single-cell plasma membrane surrounded by a dense cell wall predominantly comprises peptidoglycan. Initially, this structural feature makes *S. aureus* susceptible to specific antibiotic materials; however, over time, *S. aureus* can adapt, becoming resistant to the effects of these antibiotics.

Two potential mechanisms could be responsible for this phenomenon: either mutations in the bacterial DNA chromosome or the introduction of specific genetic material that interferes with the antibiotic's mode of action. Dat et al. [61] studied the influence of contact time on the antibacterial efficiency of Ag/rGO and observed that the density of the bacterial colony remained relatively high from 0 to 240 min, with a marked decrease starting at 720 min at a concentration of 400 μg/mL for *S. aureus*. This finding highlights the superior temporal efficacy of the TiO$_2$ matrix within the TiO$_2$/rGO composite compared with Ag alone. Although *S. aureus*, a gram-positive bacterium, is characterised by a thick cell wall, it demonstrates a shorter period required for bacterial elimination compared to *E. coli*. This difference may be explained by a greater concentration of the composite in the *S. aureus* disk diffusion medium, facilitating the more rapid and efficient penetration of TiO$_2$ through the cell walls [62]. For gram-negative bacteria, TiO$_2$/rGO is assimilated by lipopolysaccharides, thereby inflicting direct damage to the peptidoglycan layer and enhancing membrane permeability. This sequence of events culminates in the influx of TiO$_2$ ions into the cytosol, ultimately resulting in bacterial cell death. In contrast, in gram-positive bacteria, TiO$_2$/rGO directly breaches the dense peptidoglycan layer, facilitating the infiltration of TiO$_2$
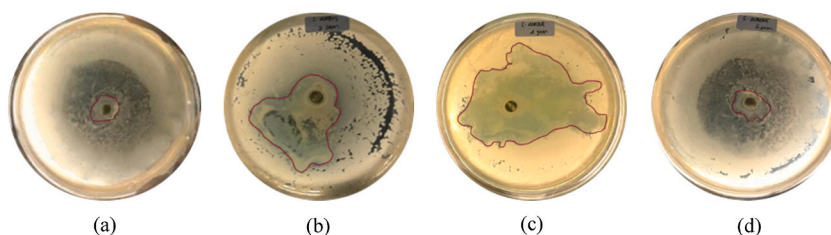

Fig. 9. Photocatalytic antibacterial process targeting *S. aureus* (a) without irradiation and with varying durations of sunlight irradiation: (a) 2 h, (b) 4 h and (c) 6 h.

ions into the cytosol, leading to similar lethal outcomes [57,63].

Photocatalytic microbial inactivation, under light exposure, stimulates ROS production on the surface of the material. The hydrophilic properties of the TiO_2/rGO surface foster interactions between the composite material and bacteria, thereby triggering a photocatalytic effect. Akhavan and Ghaderi [64] demonstrated that *E. coli* bacteria were effectively inactivated by graphene/TiO_2 thin-film nanocomposites in aqueous solutions under sunlight irradiation. The light irradiation prompts electron excitation in TiO_2, leading to the generation of ROS. Within the domain of bacterial photocatalytic inactivation, rGO serves a pivotal role akin to that in the photocatalytic degradation of organic compounds in water and wastewater, acting as a photogenerated electron acceptor.

The high conductivity of rGO expedites electron transport and mitigates the recombination of photoexcited electrons, consequently augmenting the generation of ROS. In addition, rGO extends the range of light absorption into the visible spectrum. The generated ROS disrupt bacterial cell structures, causing alterations in the organic components of the cell wall through redox reactions with released compounds. The incorporation of rGO modifications considerably enhances the quantum efficiency of the microbial inactivation process [65,66]. The interaction between ROS (H_2O_2, $O_2\bullet$, OH$\bullet$ and $H_2O\bullet$) and the sulfhydryl (–SH) groups in proteins, as well as with nucleotide base pairs within DNA, leads to DNA degradation. This bacterial photoinactivation mechanism is illustrated in Fig. 10.

In addition to the bactericidal properties of TiO_2 and rGO, the quantification of ROS is pivotal in elucidating the bacterial inactivation mechanism. ROS, which are generated both externally and internally, can inflict damage on bacterial cells. Externally originated ROS attack the cell membrane, while internally generated ROS disrupts proteins, DNA and organelles within the cell. Thabet et al. [67] emphasised the antimicrobial effects of TiO_2 on *Saccharomyces cerevisiae*, noting that TiO_2 can penetrate cellular membranes through irregularities in the cell wall, thereby causing oxidative damage. Zhou et al. [68] examined the antibacterial efficacy of a hybrid catalyst comprises rGO and TiO_2, underscoring that ROS, particularly OH$\bullet$, can disintegrate cell membrane components and compromise membrane integrity. The formation of overlapping d-π electron orbitals, facilitated by chemical bonding interactions, allows for repeated electron excitation. Electrons are then transferred to the rGO surface, reacting with oxygen and water to generate radicals. These resultant ROS are recognised for their crucial role in the observed oxidative activity. Free radicals, as reactive chemical intermediates with one or more unpaired electrons, can inflict cellular damage by donating these unpaired electrons to nearby cellular structures, leading to the oxidation of cell membrane lipids and amino acids. In photocatalytic antibacterial mechanisms, OH$\bullet$ is known to initiate lipid peroxidation in the outer cell wall, culminating in damage to cellular organelles and DNA [69,70].

Over the past decade, extensive research has focused on investigating the antimicrobial efficacy of materials based on rGO, as detailed in Table 5. Photocatalytic systems that integrate TiO_2 and rGO, employing banana peel extracts as a reducing agent, have exhibited notable success in neutralising both *E. coli* and *S. aureus*. This is evidenced by the substantial inhibition zones, measuring 35 and 22 mm for each microorganism. The achievement of the largest inhibition zone within a relatively short period and under sunlight illumination highlights the potency and effectiveness of this photocatalyst. Employing banana peels as an eco-friendly reducing agent not only enhances the economic and ecological appeal of this photocatalytic system but also ensures its sustainability and safety.

4. Conclusions

The successful biosynthesis of the TiO_2/rGO composite was realised using banana peel extracts (*Musa paradisiaca* L.). The procedure commenced with the synthesis of GO utilising a modified Tour method, proceeded with the synthesis of rGO through sonication employing banana peel extracts and culminated with the hydrothermal synthesis of TiO_2/rGO. Characterisation of the TiO_2/rGO composite through XRD analysis revealed a crystallite size of 88.505 nm for TiO_2/rGO in the rutile phase. GSA characterisation indicated the manifestation of type IV mesoporosity in TiO_2/rGO, characterised by a pore size distribution ranging from 2 to 50 nm and a surface area of 22.664 m^2/g. The FT-IR spectrum confirmed the presence of a characteristic functional group of TiO_2, notably the Ti–O–Ti bond, at a wavenumber of 648.96 cm^{-1}. UV–Vis DRS analysis revealed that TiO_2 exhibited a band gap energy of 3.15 eV, whereas TiO_2/rGO demonstrated a marginally reduced band gap energy of 3.052 eV. SEM images revealed agglomerated white lumps of TiO_2 dispersed uniformly across the rGO surface. TEM analysis delineated the structural features of TiO_2/rGO composites, showcasing sheets of rGO and spherical aggregates of TiO_2 with an average particle size of 60.5 nm. The optimal photocatalytic performance of TiO_2/rGO in degrading *E. coli* bacteria was attained under sunlight exposure for 6 h. Conversely, for *S. aureus* bacteria, the peak photocatalytic activity was observed under sunlight for 4 h.

Data accessibility statement

The datasets generated and/or analyzed during the current study will be provided by the corresponding author upon reasonable request.

CRediT authorship contribution statement

Maisari Utami: Writing – review & editing, Writing – original draft, Supervision, Software, Resources, Project administration,
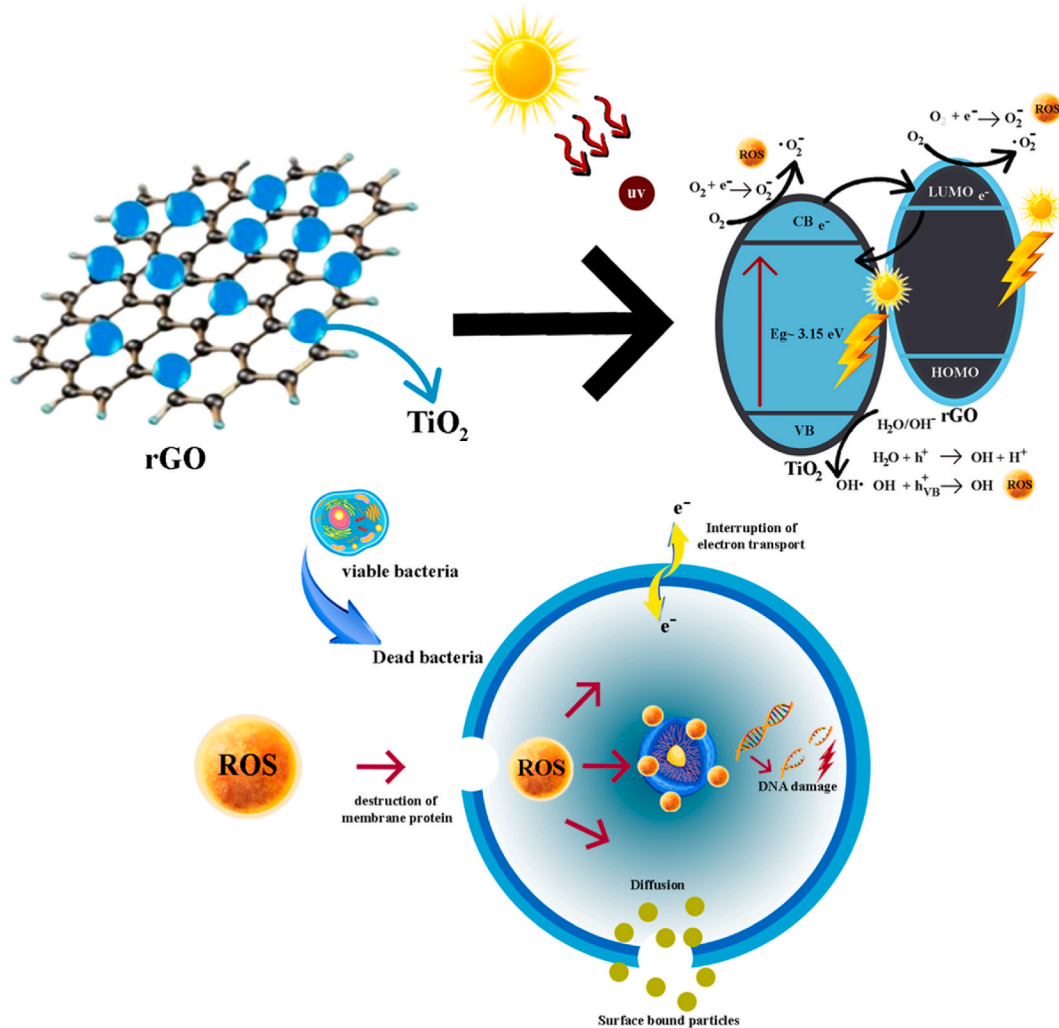
Fig. 10. Illustration of photoinactivation mechanism of *E. coli* and *S. aureus* using TiO_2/rGO.

Table 5

Comparison of photocatalytic antibacterial activity of rGO-based materials against *E. coli* and *S. aureus bacteria* from this study with previous studies.

Photocatalyst materials	Reducing GO	Light source	Contact time (h)	Bacteria	Inhibition zone diameter (mm)	Ref.
$Eu(OH)_3$/rGO	Microwave-assisted	No information	18	*E. coli*	21.2	[71]
Ce–TiO_2/rGO	Hydrazine hydrate	Visible	12	*E. coli* *S. aureus*	9.5 3	[72]
Cu_2O/rGO nanocomposite	Tagetes erecta flower extract	No information	24	*E. coli*	3	[73]
Au/rGO nanocomposite	*Piper pedicellatum* C.DC plant extract	UV	24	*S. aureus*	19.6	[74]
CS/rGO@AgNPs film	Microwave-assisted	No information	24	*E. coli* *S. aureus*	3.3 4	[75]
rGO/CuO nanocomposite	Sodium borohydride	No information	24	*E. coli* *S. aureus*	13 12	[76]
TC/rGO/PLLA nanofibers	PDA	UV	12	*E. coli* *S. aureus*	17.02 19.59	[77]
rGO-ZnS-Ag nanocomposite	DMF	Sun	24	*E. coli*	18	[78]
TiO_2/rGO	*Musa paradisiaca* L. peel extract	Sun	6 2–4	*E. coli* *S. aureus*	35 22	This Study

Methodology, Funding acquisition, Formal analysis, Data curation, Conceptualization. **Tong Woei Yenn:** Validation, Supervision, Resources, Methodology, Data curation. **Mir Waqas Alam:** Validation, Supervision, Resources, Methodology, Data curation. **Balasubramani Ravindran:** Validation, Supervision, Resources, Methodology, Data curation. **Husniati:** Husniati, Validation, Supervision, Resources, Methodology, Data curation. **Indra Purnama:** Validation, Supervision, Resources, Methodology, Data curation. **Salmahaminati:** Salmahaminati, Validation, Supervision, Resources, Methodology, Data curation. **Habibi Hidayat:** Validation, Supervision, Resources, Methodology, Data curation. **Faustine Naomi Dhetaya:** Writing – review & editing, Investigation, Formal analysis. **Siva Nur Salsabilla:** Writing – review & editing, Investigation, Formal analysis.

Declaration of competing interest

The authors declare that they have no known competing financial interests or personal relationships that could have appeared to influence the work reported in this paper.

References

[1] S. Aguilar, B. Guerrero, A. Benitez, D.R. Ramos, J.A. Santaballa, M. Canle, D. Rosado, J. Moreno-Andres, Inactivation of *E. coli* and *S. Aureus* by novel binary clay/seminconductor photocatalytic macrocomposites under UVA and sunlight irradiation, Joirnal of Environmental Chemical Engineering 1 (2023) 110813, https://doi.org/10.1016/j.jece.2023.110813.
[2] Y. Chen, X. Tang, X. Gao, B. Zhang, Y. Luo, X. Yao, Antimicrobial property and photocatalytic antibacterial mechanism of the TiO_2-doped SiO_2 hybrid materials under ultraviolet-light irradiation and visible-light irradiation, Ceram. Int. 45 (12) (2019) 15505–15513, https://doi.org/10.1016/j.ceramint.2019.05.054.
[3] J.C. Yu, W. Ho, J. Lin, H. Yip, P.K. Wong, Photocatalytic activity, antibacterial effect, and photoinduced hydrophilicity of TiO_2 films coated on a stainless steel substrate, Environ. Sci. Technol. 37 (10) (2003) 2296–2301, https://doi.org/10.1021/es0259483.
[4] E. Pérez, M.F. Torres, G. Morales, V. Murgia, E. Sham, Synthesis of N-TiO_2 effect of the concentration of nitrogen in the band gap, Procedia Materials Science 8 (2015) 649–655, https://doi.org/10.1016/j.mspro.2015.04.121.
[5] V. Caratto, L. Setti, S. Campodonico, M.M. Carnasciali, R. Botter, M. Ferretti, Synthesis and characterization of nitrogen-doped TiO_2 nanoparticles prepared by sol-gel method, J. Sol. Gel Sci. Technol. 63 (2012) 16–22, https://doi.org/10.1007/s10971-012-2756-0.
[6] N.T. Padmanabhan, N. Thomas, J. Louis, D.T. Mathew, P. Ganguly, H. John, S.C. Pillai, Graphene coupled TiO_2 photocatalysts for environmental applications: a review, Chemosphere 271 (2021) 129506, https://doi.org/10.1016/j.chemosphere.2020.129506.
[7] X. Li, J. Yu, S. Wageh, A.A. Al-Ghamdi, J. Xie, Graphene in photocatalysis: a review, Small 12 (48) (2016) 6640–6696, https://doi.org/10.1002/smll.201600382.
[8] N. Tahmasebizad, M.T. Hamedani, M. Shaban Ghazani, Y. Pazhuhanfar, Photocatalytic activity and antibacterial behavior of TiO_2 coatings co-doped with copper and nitrogen via sol-gel method, J. Sol. Gel Sci. Technol. 93 (3) (2020) 570, https://doi.org/10.1007/s10971-019-05085-1.
[9] M. Utami, S. Wang, M.M. Musawwa, T.E. Purbaningtias, M. Fitri, I. Yuspita, O.H. Abd-Elkader, K.K. Yadav, G. Munusamy-Ramanujam, D. Bang, S.W. Chan, Simultaneous photocatalytic removal of organic dye and heavy metal from textile wastewater over N-doped TiO_2 on reduced graphene oxide, Chemosphere 332 (2023) 138882, https://doi.org/10.1016/j.chemosphere.2023.139224.
[10] S. Gurunathan, J.W. Han, A.A. Dayem, V. Eppakayala, J.H. Kim, Oxidative stress mediated antibacterial activity of graphene oxide and reduced graphene oxide in pseudomonas aeruginosa, Int. J. Nanomed. 7 (2012) 5901–5914, https://doi.org/10.2147/IJN.S37397.
[11] Z. Xiong, J. Ma, W.J. Ng, T.D. Waite, X.S. Zhao, Silver-modified mesoporous TiO_2 photocatalyst for water purification, Water Res. 45 (5) (2011) 2095–2103, https://doi.org/10.1016/j.watres.2010.12.019.
[12] S.A. Akbar, F. Nanda, N. Mawaddah, M. Yuriati, Green synthesis of reduced graphene oxide using lime juice reductor from *Citrus aurantifolia*, Elkawnie: Journal of Islamic Science and Technology 5 (2) (2019) 139–146, https://doi.org/10.22373/ekw.v5i2.4948.
[13] M. Utami, S. Wang, M.M. Musawwa, M. Fitri, K. Wijaya, D. Johnravindar, O.H. Abd-Elkader, K.K. Yadav, B. Ravindran, W. jin Chung, S.W. Chang, Photocatalytic degradation of naphthol blue from Batik wastewater using functionalized TiO_2-based composites, Chemosphere 337 (2023) 139224, https://doi.org/10.1016/j.chemosphere.2023.139224.
[14] Z.Z. Yang, Q.B. Zheng, H.X. Qiu, L.I. Jing, J.H. Yang, A simple method for the reduction of graphene oxide by sodium borohydride with $CaCl_2$ as a catalyst, N. Carbon Mater. 30 (1) (2015) 41–47, https://doi.org/10.1016/S1872-5805(15)60174-3.
[15] W. Chen, L. Yan, P.R. Bangal, Chemical reduction of graphene oxide to graphene by sulfur-containing compounds, J. Phys. Chem. C 114 (47) (2010) 19885–19890, https://doi.org/10.1021/jp107131v.
[16] K. K Ai, Y. Liu, L. Lu, X. Cheng, L. Huo, A novel strategy for making soluble reduced graphene oxide sheets cheaply by adopting an endogenous reducing agent, J. Mater. Chem. 21 (10) (2011) 3365–3370, https://doi.org/10.1039/C0JM02865G.
[17] J. Yang, X. Xia, K. He, M. Zhang, S. Qin, M. Luo, L. Wu, Green synthesis of reduced graphene oxide (RGO) using the plant extract of Salvia spinosa and evaluation of photothermal effect on pancreatic cancer cells, J. Mol. Struct. 1245 (2021) 131064, https://doi.org/10.1016/j.molstruc.2021.131064.
[18] B. Qi, K. Ren, Y. Lin, S. Zhang, T. Wei, Z. Fan, Design of Layered-Stacking Graphene Assemblies as Advanced Electrodes for Supercapacitors, Particuology, 2021. https://doi:10.1016/j.partic.2021.03.001.
[19] M. Mahjuddin, B. Ochiai, Lemon juice assisted green synthesis of reduced graphene oxide and its application for adsorption of methylene blue, Technologies 9 (4) (2021) 96, https://doi.org/10.3390/technologies9040096.
[20] P. Rani, R. Dahiya, M. Bulla, R. Devi, K. Jeet, A. Jatrana, V. Kumar, Hydrothermal-assisted green synthesis of reduced graphene oxide nanosheets (rGO) using lemon (Citrus Limon) peel extract, Mater. Today: Proc. (2023), https://doi.org/10.1016/j.matpr.2023.04.419.
[21] L.H. Verastegui-Dominguez, N. Elizondo-Villarreal, D.I. Martinez-Delgado, M.A. Gracia-Pinilla, Eco-friendly reduction of graphene oxide by aqueous extracts for photocatalysis applications, J. Nanomater. 12 (21) (2022) 3882, https://doi:10.3390/nano12213882.
[22] L. Buasuwan, V. Niyomnaitham, A. Tandaechanurat, Reduced graphene oxide using an environmentally friendly banana extracts, MRS Advances 4 (38–39) (2019) 2143–2151, https://doi.org/10.1557/adv.2019.280.
[23] H. Khojasteh, H. Safajou, S. Mortazavi-Derazkola, M. Salavati-Niasari, K. Heydaryan, M. Yazdani, Economic procedure for facile and eco-friendly reduction of graphene oxide by plant extracts; a comparison and property investigation, J. Clean. Prod. 229 (2019) 1139–1147, https://doi.org/10.1016/j.jclepro.2019.04.350.
[24] S. Rai, R. Bhujel, J. Biswas, B.P. Swain, An eco-friendly method for synthesisi of Cu_2O/rGO/PANI composite using *Citrus maxima* juice for supercapacitor application, J. Mater. Sci. Mater. Electron. 32 (2021) 27937–27949, https://doi.org/10.1007/s10854-021-07175-9.
[25] A.E.D. Mahmoud, N. El-Maghrabi, M. Hosny, M. Fawzy, Biogenic synthesis of reduced graphene oxide from Ziziphus spina-christi (Christ's thorn jujube) extracts for catalytic, antimicrobial, and antioxidant potentialities, Environ. Sci. Pollut. Control Ser. 29 (59) (2022) 89772–89787, https://doi.org/10.1007/s11356-022-21871-x.
[26] S.B. Nagarajaiah, J. Prakash, Chemical composition and antioxidant potential of peels from three varieties of banana, Asian Journal of Food and Agro-Industry 4 (1) (2011) 31–46. https://www.thaiscience.info/journals/Article/AFAI/10850313.pdf.
[27] K. Devasvaran, V. Lim, Green synthesis of metallic nanoparticles using pectin as a reducing agent: a systematic review of the biological activities, Pharmaceut. Biol. 59 (1) (2021) 494–503. https://doi:10.1080/13880209.2021.1910716.

[28] H.M. Zaini, J. Roslan, S. Saallah, E. Munsu, N.S. Sualiman, W. Pindi, Banana peels as a bioactive ingredient and its potential application in the food industry, J. Funct.Foods 92 (2022) 105054, https://doi.org/10.1016/j.jff.2022.105054.

[29] S. Velumani, Phytochemical screening and antioxidant activity of banana peel, International Journal of Advance Research and Innovative Ideas in Education 2 (1) (2016) 91–102. https://www.semanticscholar.org/paper/PHYTOCHEMICAL-SCREENING-AND.

[30] M.H. Olana, F.K. Sabir, E.T. Bekele, B.A. Gonfa, *Citrus sinensis* and *Musa acuminata* Peel Waste Extract Mediated Synthesis of TiO$_2$/rGO Nanocomposites for Photocatalytic Degradation of Methylene Blue under Visible Light Irradiation, Bioinorganic Chemistry and Applications, 2022, https://doi.org/10.1155/2022/5978707.

[31] A.M. Amanulla, R. Sundaram, Green synthesis of TiO$_2$ nanoparticles using orange peel extract for antibacterial, cytotoxicity and humidity sensor applications, Mater. Today: Proc. 8 (2019) 323, https://doi.org/10.1016/j.matpr.2019.02.118, 321.

[32] A.T. Habte, D.W. Ayele, M. Hu, Synthesis and characterization of reduced graphene oxide (rGO) started from graphene oxide (GO) using the tour method with different parameters, Adv. Mater. Sci. Eng. (2019) 9, https://doi.org/10.1155/2019/5058163.

[33] G.B. Mahendran, S.J. Ramalingam, J.B.B. Rayappan, S. Kesavan, T. Periathambi, N. Nesakumar, Green preparation of reduced graphene oxide by *Bougainvillea glabra* flower extract and sensing application, J. Mater. Sci. Mater. Electron. 31 (17) (2020) 14345–14356, https://doi.org/10.1007/s10854-020-03994-4.

[34] N.R. Khalid, E. Ahmed, Z. Hong, L. Sana, M. Ahmed, Enhanced photocatalytic activity of graphene–TiO$_2$ composite under visible light irradiation, Curr. Appl. Phys. 13 (2013) 659–663, https://doi.org/10.1016/j.cap.2012.11.003.

[35] A.M. Monshi, Modified Scherrer equation to estimate more accurately nano-crystallite size using XRD, World J. Nano Sci. Eng. 2 (3) (2012) 154–160, https://doi.org/10.4236/wjnse.2012.23020.

[36] V. Paranthaman, K. Sundaramoorthy, B. Chandra, S.P. Muthu, P. Alagarsamy, R. Perumalsamy, Investigation on the performance of reduced graphene oxide as counter electrode in dye sensitized solar cell applications, Physica Status Solid (a) 215 (18) (2018) 1800298, https://doi.org/10.1002/pssa.201800298.

[37] A. Alazmi, O. El Tall, S. Rasul, M.N. Hedhili, S.P. Patole, P.M.F.J. Costa, A process to enhance the specific surface area and capacitance of hydrothermally reduced graphene oxide, Nanoscale 8 (41) (2016) 17782–17787. https://doi:10.1039/c6nr04426c.

[38] H. Xia, Y. Wang, J. Lin, L. Lu, Hydrothermal synthesis of MnO$_2$/CNT nanocomposite with a CNT core/porous MnO$_2$ sheath hierarchy architecture for supercapacitors, Nanoscale Res. Lett. 7 (2012) 1–10, https://doi.org/10.1186/1556-276X-7-33.

[39] H.C. Youn, S.M. Bak, M.S. Kim, C. Jaye, D.A. Fischer, C.W. Lee, X.Q. Yang, K.C. Roh, K.B. Kim, High-surface-area nitrogen-doped reduced graphene oxide for electric double-layer capacitors, ChemSusChem 8 (11) (2015) 1875–1884. https://www.osti.gov/pages/servlets/purl/1177001.

[40] V.B. Mohan, K. Jayaraman, D. Bhattacharyya, Brunauer–Emmett–Teller (BET) specific surface area analysis of different graphene materials: a comparison to their structural regularity and electrical properties, Solid State Commun. 114004 (2020). https://doi.org/10.1016/j.ssc.2020.114004.

[41] M. Ruidíaz-Martínez, M.A. Álvarez, M.V. López-Ramón, G. Cruz-Quesada, J. Rivera-Utrilla, M. Sánchez-Polo, Hydrothermal synthesis of rGO-TiO$_2$ composites as high-performance UV photocatalysts for ethylparaben degradation, Catalysts 10 (5) (2020) 520.

[42] T.Y. Zhang, D. Zhang, Aqueous colloids of graphene oxide nanosheets by exfoliation of graphite oxide without ultrasonication, Bull. Mater. Sci. 34 (2011) 25–28, https://doi.org/10.1007/s12034-011-0048-x.

[43] L. Shahriary, A.A. Athawale, Graphene oxide synthesized by using modified hummers approach, International Journal of Renewable Energy and Environmemtal Engineering 2 (1) (2014) 58–63.

[44] T.F. Emiru, D. Ayele, Controlled synthesis, characterization and reduction of graphene oxide: a convenient method for large scale production, Egyptian Journal of Basic and Applied Sciences 4 (1) (2017) 74–79. https://doi:10.1016/j.ejbas.2016.11.002.

[45] Z. Kang, H. Gao, Z. Hu, X. Jia, D. Wen, Ni–Fe/reduced graphene oxide nanocomposites for hexavalent chromium reduction in an aqueous environment, ACS Omega 7 (5) (2022) 4041–4051, https://doi.org/10.1021/acsomega.1c05273.

[46] R.K. Nainani, P. Thakur, Facile synthesis of TiO$_2$-RGO composite with enhanced performance for the photocatalytic mineralization of organic pollutants, Water Sci. Technol. 73 (8) (2016) 1927–1936.

[47] Y. Liu, Hydrothermal synthesis of TiO$_2$–RGO composites and their improved photocatalytic activity in visible light, RSC Adv. 4 (68) (2014) 36040–36045, https://doi.org/10.1002/smll.201600382.

[48] J.O. Olowoyo, M. Kumar, B. Singh, V.O. Oninla, J.O. Babalola, H. Valdés, A.V. Vorontsov, U. Kumar, Self-assembled reduced graphene oxide-TiO$_2$ nanocomposites: synthesis, DFTB+ calculations, and enhanced photocatalytic reduction of CO$_2$ to methanol, Carbon 147 (2019) 385–397, https://doi.org/10.1016/j.carbon.2019.03.019.

[49] L. Yu, B. Tang, Photocatalytic degradation of phenolic compounds from wastewater using titanium dioxide@reduced graphene oxide (TiO$_2$@rGO) nanocomposites, Int. J. Electrochem. Sci. 16 (9) (2021). http://electrochemsci.org/papers/vol16/210915.pdf.

[50] Y. Jin, Y. Zheng, S.G. Podkolzin, W. Lee, Band gap of reduced graphene oxide tuned by controlling functional groups, J. Mater. Chem. C 8 (14) (2020) 4885–4894, https://doi.org/10.1039/C9TC07063J.

[51] A.T. Smith, A.M. LaChance, S. Zeng, B. Liu, L. Sun, Synthesis, properties, and applications of graphene oxide/reduced graphene oxide and their nanocomposites, Nano Materials Science 1 (1) (2019) 31–47, https://doi.org/10.1016/j.nanoms.2019.02.004.

[52] B. Qi, K. Ren, Y. Lin, S. Zhang, T. Wei, Z. Fan, Design of Layered-Stacking Graphene Assemblies as Advanced Electrodes for Supercapacitors, Particuology, 2021. https://doi:10.1016/j.partic.2021.03.001.

[53] Z. Li, R.J. Young, R. Wang, F. Yang, L. Hao, W. Jiao, W. Liu, The role of functional groups on graphene oxide in epoxy nanocomposites, Polymer 54 (21) (2013) 5821–5829. https://doi.org/10.1016/j.polymer.2013.08.026.

[54] D.T. Tran, rGO/persulfate metal-free catalytic system for the degradation of tetracycline: effect of reaction parameters, Mater. Res. Express 7 (7) (2020) 075501, https://doi.org/10.1088/2053-1591/ab9e47.

[55] H.S. Hussein, H.H. Shaarawy, N.H. Hussien, S.I. Hawash, Preparation of nano-fertilizer blend from banana peels, Bull. Natl. Res. Cent. 43 (2019) 1–9, https://doi.org/10.1186/s42269-019-0058-1.

[56] O. Zuas, H. Budiman, Synthesis of nanostructured copper-doped titania and its properties, Nano-Micro Lett. 5 (2013) 26–33, https://doi.org/10.1007/BF03353728.

[57] D. Xu, P. Wang, B. Shen, Development of TiO$_2$-reduced graphene oxide nanocomposites and their enhanced photocatalytic and photovoltaic performance, Dig. J. Nanomater. Biostruct. 11 (1) (2016). https://www.chalcogen.ro/15_Xu.pdf.

[58] M. Wei, L. Qiao, H. Zhang, S. Karakalos, K. Ma, Z. Fu, M.T. Swihart, G. Wu, Engineering reduced graphene oxides with enhanced electrochemical properties through multiple-step reductions, Electrochim. Acta 258 (2017) 735–743.

[59] H.J. Kim, Y.G. Shul, H. Han, Photocatalytic properties of silica supported TiO$_2$, Top. Catal. 35 (2005) 287–295, https://doi.org/10.1007/s11244-005-3836-y.

[60] M.A.E. Wafi, M.A. Ahmed, H.S. Abdel-Samad, H.A.A. Medien, Exceptional removal of methylene blue and p-aminophenol dye over novel TiO$_2$/rGO nanocomposites by tandem adsorption-photocatalytic processes, Materials Science for Energy Technologies 5 (2022) 217–231, https://doi.org/10.1016/j.mset.2022.02.003.

[61] N.M. Dat, V.N.P. Linh, N.T.L. Phuong, L.N. Quan, N.T. Huong, L.A. Huy, N.H. Hieu, The Effects of Concentration, Contact Time, and pH Value on Antibacterial Activity of Silver Nanoparticles Decorated Reduced Graphene Oxide, Materials Technology, 2019, pp. 1–8. https://doi.org/10.1080/10667857.2019.1630898.

[62] Y.N. Slavin, J. Asnis, U.O. Häefeli, H. Bach, Metal nanoparticles: understanding the mechanisms behind antibacterial activity, J. Nanobiotechnol. 15 (1) (2017) 20.

[63] K.S.V.K. Rao, P.R. Reddy, K.M. Rao, S.P. Kumar, A green approach to synthesize silver nanoparticles from natural polymer for biomedical application, Indian J. Adv. Chem. Sci. 3 (2015) 340–344.

[64] O. Akhavan, E. Ghaderi, Photocatalytic reduction of graphene oxide nanosheets on TiO$_2$ thin film for photoinactivation of bacteria in solar light irradiation, J. Phys. Chem. C 113 (47) (2009) 20214–20220. https://doi.org/10.1021/jp906325q.

[65] E. Kusiak-Nejman, A.W. Morawski, TiO$_2$/graphene-based Nanocomposites for Water Treatment: A Brief Overview of Charge Carrier Transfer, Antimicrobial and Photocatalytic Performance, Applied Catalysis B: Environmental, 2019. https://doi:10.1016/j.apcatb.2019.04.055.

[66] L. Ayala-Fonseca, E. Ameiva, C. Rodriguez-Gonzales, C. Angele- Chavez, E. De la Rossa, V. Castano, P. Salas, Enhanced Raman effect of solvothermal synthesized reduced graphene oxide/titanium dioxide nanocomposite, ChemistrySelect 5 (2020) 3789–3797, https://doi.org/10.1002/slct.202000335.

[67] S. Thabet, F. Simonet, M. Lemaire, C. Guillard, P. Cotton, Impact of photocatalysis on fungal cells: Depiction of cellular and molecular effects on *Saccharomyces cerevisiae*, Appl. Environ. Microbiol. 80 (24) (2014) 7527–7535. https://doi:10.1128/aem.02416-14.

[68] X. Zhou, M. Zhou, S. Ye, Y. Xu, S. Zhou, Q. Cai, Y. Li, Antibacterial activity and mechanism of the graphene oxide (rGO)-modified TiO$_2$ catalyst against *Enterobacter hormaechei*, Int. Biodeterior. Biodegrad. 162 (2021). https://doi:10.1016/j.ibiod.2021.105260.

[69] J.P. Carroll, E. Panaitescu, B. Quilty, L. Wang, L. Menon, S.C. Pillai, Antimicrobial properties of highly efficient photocatalytic TiO$_2$ nanotubes, Appl. Catal. B Environ. 176–177 (2015) 70–75, https://doi.org/10.1016/j.apcatb.2015.03.029.

[70] Y. Chen, X. Tang, X. Gao, B. Zhang, Y. Luo, X. Yao, Antimicrobial property and photocatalytic antibacterial mechanism of the TiO$_2$-doped SiO$_2$ hybrid materials under ultraviolet-light irradiation and visible-light irradiation, Ceramic International Journal 45 (12) (2019) 15505–15513, https://doi.org/10.1016/j.ceramint.2019.05.054.

[71] K.Y. Shih, S.C. Yu, Microwave-assisted rapid synthesis of Eu(OH)$_3$/RGO nanocomposites and enhancement of their antibacterial activity against *Escherichia coli*, Materials 15 (1) (2021) 43, https://doi.org/10.3390/ma15010043.

[72] L. Behera, B. Barik, S. Mohapatra, Improved photodegradation and antimicrobial activity of hydrothermally synthesized 0.2 Ce-TiO$_2$/RGO under visible light, Colloids Surf. A Physicochem. Eng. Asp. 620 (2021) 126553, https://doi.org/10.1016/j.colsurfa.2021.126553.

[73] M.N. Rani, M. Murthy, N.S. Shree, S. Ananda, S. Yogesh, R. Dinesh, Cuprous oxide anchored reduced graphene oxide ceramic nanocomposite using *Tagetes erecta* flower extract and evaluation of its antibacterial activity and cytotoxicity, Ceram. Int. 45 (18) (2019) 25020–25026, https://doi.org/10.1016/j.ceramint.2019.04.195.

[74] I. Saikia, S. Sonowal, M. Pal, P.K. Boruah, M.R. Das, C. Tamuly, Biosynthesis of gold decorated reduced graphene oxide and its biological activities, Mater. Lett. 178 (2016) 239–242, https://doi.org/10.1016/j.matlet.2016.05.011.

[75] B. Gu, Q. Jiang, B. Luo, C. Liu, J. Ren, X. Wang, X. Wang, A sandwich-like chitosan-based antibacterial nanocomposite film with reduced graphene oxide immobilized silver nanoparticles, Carbohydr. Polym. 260 (2021) 117835, https://doi.org/10.1016/j.carbpol.2021.117835.

[76] S. Siddique, M. Waseem, T. Naseem, A. Bibi, M. Hafeez, S.U. Din, S. Haq, S. Qureshi, Photocatalytic and anti-microbial activities of rGO/CuO nanocomposite, J. Inorg. Organomet. Polym. Mater. 31 (2021) 1359–1372, https://doi.org/10.1007/s10904-020-01760-x.

[77] B. Li, F. Xiong, B. Yao, Q. Du, J. Cao, J. Qu, W. Feng, H. Yuan, Preparation and characterization of antibacterial dopamine-functionalized reduced graphene oxide/PLLA composite nanofibers, RSC Adv. 10 (32) (2020) 18614–18623, https://doi.org/10.1039/D0RA0322.

[78] H. Naeem, H.M. Tofil, M. Soliman, A. Hai, S.H.H. Zaidi, N. Kizilbash, D. Alruwaili, M. Ajmal, M. Siddiq, Reduced graphene oxide-zinc sulfide nanocomposite decorated with silver nanoparticles for wastewater treatment by adsorption, photocatalysis and antimicrobial action, Molecules 28 (3) (2023) 926, https://doi.org/10.3390/molecules28030926.